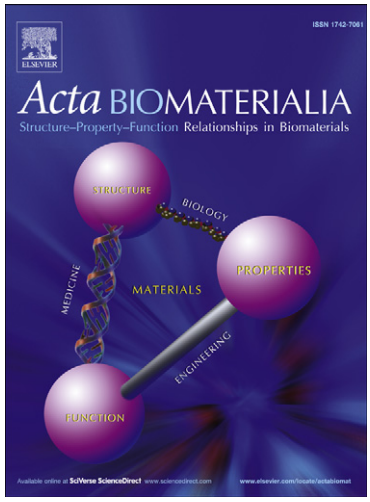

Crystallization of bioinspired citrate-functionalized nanoapatite with tailored carbonate content

José Manuel Delgado-López, Michele Iafisco, Isaac Rodríguez, Anna Tampieri, María Prat, Jaime Gómez-Morales

PII: S1742-7061(12)00204-8
DOI: http://dx.doi.org/10.1016/j.actbio.2012.04.046
Reference: ACTBIO 2201

To appear in: *Acta Biomaterialia*

Received Date: 12 February 2012
Revised Date: 26 March 2012
Accepted Date: 30 April 2012

Please cite this article as: Delgado-López, J.M., Iafisco, M., Rodríguez, I., Tampieri, A., Prat, M., Gómez-Morales, J., Crystallization of bioinspired citrate-functionalized nanoapatite with tailored carbonate content, *Acta Biomaterialia* (2012), doi: http://dx.doi.org/10.1016/j.actbio.2012.04.046

ELSEVIER

Available online at www.sciencedirect.com

ScienceDirect

Acta Biomaterialia 00 (2012) 000–000

Acta Biomaterialia

Crystallization of bioinspired citrate-functionalized nanoapatite with tailored carbonate content

José Manuel Delgado-López*[,a], Michele Iafisco[b,c], Isaac Rodríguez[a], Anna Tampieri[d], María Prat[c], Jaime Gómez-Morales[a]

[a]*Laboratorio de Estudios Cristalográficos, IACT (CSIC-UGR). Avda. de las Palmeras, 4. 18100 Armilla, Granada, Spain.*

[b]*Dipartimento di Chimica "G. Ciamician". Alma Mater Studiorum, Università di Bologna. Via Selmi 2, 40126 Bologna, Italy.*

[c]*Dipartimento di Scienze Mediche. Università del Piemonte Orientale. Via Solaroli 4, 28100 Novara, Italy.*

[d]*Institute of Science and Technology for Ceramic (CNR), Via Granarolo 64, 48018 Faenza (RA), Italy.*

**Email: jmdl@lec.csic.es*

Abstract

Novel citrate-functionalized carbonate-apatite nanoparticles with mean lengths ranging from 20 to 100 nm were synthesized by a thermal-decomplexing batch method. Needle-like and plate-shaped morphologies were obtained in the absence and in the presence of sodium carbonate in the precipitation medium, respectively. The precipitation time and the presence of sodium carbonate strongly affect the chemical composition as well as the dimensions and the crystallinity of nanoparticles. At short precipitation time, poorly crystalline 100 nm-mean length apatites with low carbonation degree (1.5% w/w, mainly in B-position) and high citrate content (5.9% w/w) were precipitated. This citrate content is close to that recently measured on bone apatite. When increasing the precipitation time up to 96 hours the mean length and the citrate content progressively decrease and at the same time the nanoparticles become more crystalline. They were composed of a well-ordered carbonate-substituted apatitic core embedded in a non-apatitic hydrated layer containing citrate ions. This layer progressively transforms into more stable apatite domain upon maturation in aqueous media. The nanoparticles displayed excellent compatibility properties in cell biology systems, since they were not cytotoxic to a mouse carcinoma cell line, when added until a final concentration of 100 μg mL^{-1}. This work will provide new insights on the role of citrate in the crystallization of nanoapatites. Moreover, the synthesized nanoparticles are promising materials to be used as nano-carriers for local targeted drug delivery systems as well as building blocks for the preparation of nanostructured scaffolds for cells in bone tissue engineering.

Keywords: Calcium Phosphates; Hydroxyapatite; Carbonate; Nanocrystals; Citrate.

1. Introduction

Hydroxyapatite [(HA), $Ca_5(PO_4)_3(OH)$] is the most stable calcium phosphate phase in physiological conditions and the model compound to designate the mineral component of bone and dentin [1, 2]. Biological apatites are calcium deficient crystals with Ca/P ratio lower than the theoretical value of stoichiometric hydroxyapatite (1.67). [1, 2] They are plate-shaped nanoparticles with a length of about 30-50 nm, width of 30-50 nm and thickness of 2-10 nm [2, 3]. In addition, they usually present several foreign ions into the crystalline structure such as carbonate (4-6%), Na (0.9%) and Mg (0.5%) among others [2, 3].

Apatite crystallization has been the object of extensive research in numerous interdisciplinary areas to better understand its formation mechanism in natural mineralization processes [4] as well as to investigate its preparation as biomaterial due to its well known biomedical properties [5]. Many different methodologies have been proposed to prepare nanosized and/or nanocrystalline apatites both in the absence and in the presence of additives [6]. However, the synthesis of apatite presenting characteristics similar to those of biological bone in term of sizes, specific surface area, carbonation degree and surface composition is still a technological challenge.

It is well accepted that the organic component of bone acts as an important regulator of lattice orientation, particle size, and size distribution in biomineralization processes [7, 8]. However the molecular recognition details at the organic-inorganic interfaces are still not completely understood. In the last years, most researchers were focused on the effects of aminoacids [9] and biological macromolecules such as carboxylate-rich proteins [10-12] on calcium phosphates nucleation and growth but they disregarded the role of small organic molecules such as citrate. Citrate ions are Ca-complexing agents, biocompatible, and inhibitors of apatite crystals growth by strongly interacting with the surface [13, 14]. Recently, new insight about the role of citrate is emerging, as illustrated by the study of Hu *et al*. [14], who reported that strongly bound citrate molecules interfere with the crystal thickening and stabilize the size of the nanoapatites in bone. They also demonstrated by means of advanced multi-NMR spectroscopy that citrate, strongly immobilized on bone apatite surfaces, accounts for 5.5% wt. of the organic bone matter [14]. According to this, the density of the citrate coverage is approximately one molecule per 2 nm^2, which implies that approximately one sixth of the available apatite surface area in bone is covered by citrate molecules [14]. Recently, Xie and Nancollas [15] have reviewed the most interesting works on the role of citrate binding on apatite surface to tailor the nanocrystal size, and they hypothesized that this strategy inspired from nature can be a powerful tool to control the synthesis of this material.

The aim of the present work was to synthesize biomimetic citrate-functionalized carbonate-apatite nanocrystals with tailored citrate surface composition and carbonate content by using a thermal-decomplexing batch method [13]. Furthermore, a complete crystal structural evolution of these materials with the precipitation time up to 96 hours was

investigated. This work will provide new insights on the role of citrate ions in the crystallization of nanoapatites and will increase the knowledge in the field of bone calcification. Furthermore, the nanoparticles are promising materials to be used as nano-carriers for local targeted drug delivery systems [16] as well as scaffolds for cells in bone replacement [17].

2. Materials and methods

2.1. Materials

Calcium chloride dihydrate ($CaCl_2.2H_2O$, Bioxtra, ≥ 99,0 % pure), sodium citrate tribasic dihydrate ($Na_3(Cit).2H_2O$ where Cit=citrate=$C_6H_5O_7$, ACS reagent, ≥ 99,0 % pure), sodium phosphate dibasic (Na_2HPO_4, ACS reagent, ≥ 99,0 % pure) and sodium carbonate monohydrate ($Na_2CO_3.H_2O$, ACS reagent, 99.5% pure) were supplied by Sigma-aldrich. Ultrapure water (0.22 μS, 25 °C, MilliQ©, Millipore) was used.

2.2. Crystallization method

Nanoparticles were precipitated by a batch heating method according to the procedure developed by López-Macipe *et al* [13]. Two solutions (1:1 v/v, 200 mL total) of (i) 0.1 M $CaCl_2$ + 0.4 M $Na_3(Cit)$ and (ii) 0.12 M Na_2HPO_4, + x mM Na_2CO_3 (x = 0 or 100) were mixed at 4 ºC. In the experiments without Na_2CO_3, the resulting precipitate will be referred to as Ap, whereas in the experiments with x=100 mM Na_2CO_3 the resulting material will be referred to as cAp due to the presence of higher amount of carbonate ions in the lattice. In both cases the pH was adjusted to 8.5 with HCl. Citrate anions were used as calcium complexing agent to prepare homogeneous metastable solutions in order to avoid the instantaneous calcium carbonate or calcium phosphate precipitation. The mixture was then introduced in a 250 mL round-bottom flask, sealed with a glass stopper and immersed in a water bath at 80 °C. The experiments were performed at different times ranging from 5 minutes to 96 hours. An additional experiment to the set with x=100 mM Na_2CO_3 was carried out by collecting the powder just after immersing the metastable solution in the flask at 80ºC (time 0). After the precipitation, the particles were repeatedly washed with ultrapure water (MilliQ©, Millipore) by centrifugation, and then dried at 37 ºC.

2.3. Characterization techniques

A hot line probe (Sentron) was used to measure the pH evolution of the reaction mixture during the precipitation at 80 ºC. The activity of the species in solution as a function of both the temperature and the pH were calculated by using the Visual MINTEQ 3.0 speciation software [18] (See supporting information for more details). Transmission

electron microscopy (TEM) observations as well as selected area electron diffraction (SAED) and energy-dispersive X-ray spectroscopy (EDS) analysis were performed with a STEM Philips CM 20 microscope operating at 80 kV. The powder samples were ultrasonically dispersed in ultrapure water and then few droplets of the slurry were deposited on conventional copper microgrids. The Ca/P ratio was determined by inductively coupled plasma-optical emission spectrometry (ICP-OES, Liberty 200, Varian, Clayton South, Australia). Samples were dissolved in 1% wt. ultrapure nitric acid. The following analytical wavelengths were chosen: Ca 422 nm, P 213 nm. The analyses were carried out 3 times on 3 different synthesis products. Thermogravimetric analysis (TGA) was carried out using a Thermal Analysis SDT Q 600 (TA Instruments, New Castle, DE, USA). Heating was performed in a nitrogen flow (100 mL min^{-1}) using an alumina sample holder. Temperature was increased from room temperature to 1200 °C with a heating rate of 10 °C min^{-1}. Samples weight approximately 5 mg. The analyses were carried out 3 times on the same synthesis product. Data from ICP and TGA are presented as mean value ± Standard Deviation. Data obtained from experiments were compared by a two-tailed test. Significance level was considered for $p < 0.05$. X-Ray Powder diffraction (XRPD) patterns were collected using a Cu Kα radiation (λ=1.5418Å) on a PANalytical X'Pert PRO diffractometer equipped with a PIXcel detector operating at 45 kV and 40 mA. For the diffracted beam an automatic-variable anti-scatter slit with an irradiated length of 10 mm was used. The 2θ range was from 5° to 80° with a step size of (2θ) 0.039°.

The average size of crystal domains along the apatite axis directions ($D_{[002]}$) and ($D_{[310]}$) were calculated applying the Scherrer equation [19] (1):

$$D_{([hkl])}=0.9\lambda/[\cos\theta(\sqrt{(\Delta_r^2)-\Delta_0^2})] \quad (1)$$

where θ is the diffraction angle for plane (hkl), Δ_r and Δ_0 the widths in radians of reflection hkl at half height for the synthesized and pure inorganic hydroxyapatite (standard reference material, calcium hydroxyapatite, National Institute of Standards & Technology), respectively, and λ=1.5405 Å. The XRPD patterns were background corrected before the Scherrer analysis. Fourier Transform Infrared (FTIR) spectra were recorded on a Thermo Nicolet 380 FTIR spectrometer. Each powdered sample (~ 1 mg) was mixed with about 200 mg of anhydrous KBr and pressed into 7 mm diameter discs. Pure KBr discs were used as background. The infrared spectra were registered from 4000 cm^{-1} to 400 cm^{-1} with a resolution of 4 cm^{-1}. Raman spectra were collected with a LabRAM-HR spectrometer (Jobin-Yvon, Horiba, Japan). The excitation line was provided by a diode laser emitting at a wavelength of 785.4 nm and a Peltier cooled charge-couple device (CCD) (1064 x 256 pixels) were used as detector. Spectrometer resolution is higher than 3 cm^{-1}. For each acquisition and depending on the quality of the spectra, signal averaging of two or three spectra and acquisition time between 40 and 400 s was performed. The Raman intensity was represented as counts per seconds (cps).

2.4. Cytotoxicity test

4T1 mouse carcinoma cells (ATCC CRL-2539™) were incubated (2 x 10^3/0.4 cm^2 microwell) during 24 hours and afterwards, different concentrations of cAp and Ap nanoparticles, ranging from 1 to 100 µg mL^{-1}, were added in 100 µL. After 2 days incubation, cells viability was evaluated by the 3-(4,5-Dimethylthiazol-2-yl)-2,5-diphenyltetrazolium bromide) (MTT, Sigma) colorimetric assay. Briefly, 20 µl of MTT solution (5 mg mL^{-1} in a PBS solution) were added to each wells containing cells. The plate was then incubated for 3 hours at 37ºC. Afterwards, 0.2 N HCl in isopropanol was added to dissolve formazan crystals. Optical density was measured in a multiwell reader (2030 Multilabel Reader Victor TM X4, PerkinElmer) at 570 nm. Experiments were performed 4 times using 3 replicates for each samples.

3. Results

The activity of the Ca-citrate complex as well as the main calcium, citrate and phosphate ion pairs in the mother solution with and without sodium carbonate, as a function of the temperature is plotted in Figure 1. The activities of the other Ca-complexes such as $CaCl^+$ and CaH(Cit) were negligible and for the sake of simplicity were not plotted. Figure 1 clearly shows that the Ca-Citrate complex ($[Ca(Cit)]^-$) is destabilized by the temperature increase both with and without sodium carbonate. This fact allows a gradual and homogeneous release of Ca^{2+} ions into the solution, which in the presence of phosphate groups leads to the formation of calcium phosphate aqueous species such as $[CaPO_4]^-$ and $[CaHPO_4]^0$ and then to the formation of a calcium phosphate precipitate. The above species were previously proposed as growth units for hydroxyapatite [20]. Figure 1(b) shows also the increase in the activity of the carbonate species $[CaCO_3]^0$ with the temperature indicating that $CaCO_3$ could also precipitate in these

experiments. However, we did not find evidences of the $CaCO_3$ precipitation since the solubility product of any $CaCO_3$ phase is much higher than the solubility product of hydroxyapatite.

3.1. *Morphological characterization by TEM*

Figure 2 shows TEM micrographs of the Ap (a, c and e) and cAp (b, d, f) particles precipitated at different times. Apatite crystals grew with their longest axis parallel to the *c* crystallographic axis similarly to the ones crystallized by other methods [6, 9, 21]. The particles precipitated after 5 minutes show diffuse borders and poor crystallinity degree as pointed out by the SAED patterns (insets in Figures 2 (a) and (b)). On the contrary, thin needle-like nanoparticles with progressively better-defined border were found when increasing the precipitation time. The SAED patterns collected for the particles crystallized after 96 hours (insets in Figure 2 (e) and (f)) were similar to those reported for crystalline hydroxyapatite [22, 23]. They show the typical reflections 002, 112 and 004 at *d*-spacing equal to 3.44 Å, 2.75 Å and 1.72 Å, respectively (ASTM Card file No. 9-432). The nanoparticles precipitated at short crystallization time are probably composed of a well-ordered apatitic core embedded in a "non-apatitic hydrated layer" as suggested by Rey *et al*. [24, 25]. Actually, one of the most interesting characteristics of biomimetic apatite nanocrystals is the existence of a hydrated surface layer, composed of calcium, phosphate and carbonate species [24, 25] and, in our experiments, also citrate. This surface layer is well developed in freshly formed precipitates and becomes progressively transformed into a more stable apatitic lattice upon maturation in aqueous media [24, 25]. Occasionally, at shorter precipitation times, few platelets (ranging from 1 to 10 µm, not shown) of octacalcium phosphate (OCP) were detected [26].

The mean length (L) along the longest axis, the mean width (W) and the mean aspect ratio (R, i.e., the ratio between L and W) of Ap and cAp nanoparticles crystallized at different times were estimated from TEM observations. The L values of Ap nanoparticles decreased from 100 nm to 45 nm in the first hour and then gradually increased up to 105 nm after 96 hours. The same trend was observed for the width (from 21 to 12 nm and then to 15 nm). On the contrary, L of the cAp nanocrystals strongly reduced during the first hour, then slightly increased up to 60 nm and after that underwent a slight reduction with the time. In contrast to Ap, R values for cAp become lower with the time. Therefore, the presence of sodium carbonate in the solution leads to the formation of smaller nanoparticles with lower aspect ratio (*i.e.* more isometric particles), in comparison with the Ap, irrespective of the precipitation time. It has to be considered that the uncertainties in the determination of accurate dimensions of apatites nanoparticles from TEM observations (table 1) is mainly due to agglomeration process which makes it difficult to observe individual particles. Nonetheless, we have detected that the aggregation tendency decreases when increasing the precipitation time as depicted in Figure 2. However, to determine the dimensional distributions only non-aggregated nanoparticles were considered.

3.2. *Crystallographic characterization by X-ray Diffraction*

Figures 3(a) and 3(b) represent the X-ray diffraction patterns of Ap and cAp, respectively, precipitated after 5 minutes and 96 hours. They display the characteristic diffraction reflections of hydroxyapatite single phase (ASTM

Card file No. 9-432). Any peak assignable to OCP phase (ASTM Card file No. 26-1056) at low diffraction angles was found (data not shown) even at earlier precipitation times. The most intense peaks appear at 25.88º (related with the 002 planes) and around 32º (broad band due to the triplet 211, 112 and 300). The diffraction peaks are broad and poorly defined. This broadness is more evident at shorter crystallization times suggesting a relatively lower degree of crystallinity and nano-dimensions [25] in accordance with the above described SAED results.

The diffraction pattern of the powders precipitated at time 0 in the presence of Na_2CO_3 were characterized by the absence of reflections. The Raman spectrum shows a broad peak at 953 cm^{-1} that identifies this precipitate as pure amorphous calcium phosphates (ACP) (Figure SP1).

The average size of crystal domains along the *c*-axis ($D_{[002]}$) and the *a*-*b* plane (orthogonal to the *c*-axis, $D_{[310]}$), calculated by the Scherrer's equation using the width at half height for the respective reflections 002 and non-overlapped 310, are shown in table 1. For both type of apatites, the values of $D_{[002]}$ at short times were close to those of bone apatite (around 20 nm) [27]. $D_{[002]}$ strongly increased with time whereas $D_{[310]}$ slightly raised according to a preferential growth along the *c*-axis. Additionally, the $D_{[002]}$ values as well as the $D_{[002]}/ D_{[310]}$ ratio were lower for cAp in agreement with the TEM observations. This finding is explained by the incorporation of carbonate ions into the lattice, as previously reported by other authors [28-30]. It has to be highlighted that $D_{[002]}$ and $D_{[310]}$ values correspond to dimensions of crystallite domains. In contrast, L and W measurements refer to the dimensions of projected images of nanoparticles as observed by TEM.

3.3. Compositional analysis by TGA and ICP-OES

The chemical composition of the nanocrystals was analyzed by ICP and TGA (table 2). The Ca/P ratios estimated by ICP for the Ap and cAp nanocrystals were slightly lower than the stoichiometric value (1.67) irrespective of the precipitation time. They were slightly higher for the cAp since carbonate was replacing phosphates groups [30]. Therefore, this method yields Ca-deficient apatites with Ca/P ratio close to the biological ones (1.5) [1, 2]. TGA analysis mainly shows four weight losses (Figure SP2): i) from room temperature to 200 °C due to the adsorbed water, ii) from 200 °C to 400 °C related to structural water, iii) from 400 to 600 °C due to the citrate as well as the small amount of non-apatitic HPO_4 ions and iv) from 600 to 1000 °C corresponding to the carbonate ions [31]. These assignments are well supported by the FTIR spectra collected after sample annealing at 400 °C and 600 °C (Figure SP3). The amount of structural water as well as of the adsorbed citrate decreased with the precipitation time in both samples, probably because of a progressive modification from non-apatitic chemical environments to apatitic ones and a gradual dissolution of the hydrated layer with the time. The citrate content is close to the one recently measured in bone apatite surface [14]. The presence of carbonate in the Ap (around 1%) was mainly due to dissolved CO_2 in the mother solution and to CO_2 adsorbed onto the surface materials during the storage. The highest carbonate content in the cAp was obtained after 24 hours which is explained by a higher activity of carbonated species in the solution at that time. Indeed, a plot of the activities of carbonated species (CO_3^{2-}, $[CaCO_3]^0$ and $[NaCO_3]^-$) as a function of time (Figure 4) showed the maximum value at about 24 hours.

3.5. Spectroscopic characterization

The nanocrystals were characterized by FTIR and Raman spectroscopies. Figure 5 represents the FTIR spectra of cAp crystallized at 5 minutes and 48 hours. They displayed a main broad band at *ca.* 1030 cm^{-1} with shoulders at *ca.* 1046 and 1075 cm^{-1} due to the triply degenerated asymmetric stretching mode of the apatitic PO_4 groups (ν_3PO_4). This band is slightly red-shifted with respect to that of stoichiometric hydroxyapatite, most likely due to the presence of CO_3^{2-}, and/or HPO_4^{2-} ions incorporated into the crystal lattice [32, 33]. Other features emerge at *ca.* 961 cm^{-1} (symmetric stretching mode of the apatitic PO_4 groups, ν_1PO_4) and at *ca.* 603, 576 (as a shoulder) and 565 cm^{-1} (triply degenerated bending mode of the same groups, ν_4PO_4) [32, 33]. FTIR spectra confirm the absence of OCP in agreement with the XRPD data. The spectra of the Ap precipitated at higher times also show bands at 3567 (Figure SP4) and 631 cm^{-1} corresponding to the stretching and librational modes of the apatitic hydroxyl groups, respectively [32]. On the contrary, they were nearly negligible in the spectra of cAp mainly due to the substitution of the OH groups by CO_3^{2-} in the crystal lattice (A-type carbonation) [34]. This finding was confirmed by the presence of carbonate bands at *ca.* 1550, 1465 (as a shoulder) and 880 cm^{-1} (Figure 5). In addition, the existence of B-type carbonate substitutions (CO_3 occupying PO_4 sites) is witnessed by the bands at *ca.* 1452, 1415 and 873 cm^{-1} [34].

The spectrum of the particles after 5 minutes in Figure 5 shows a shoulder at 534 cm^{-1} in the ν_4PO_4 domain. Rey *et al.* [24] assigned this feature to phosphate and/or hydrogenphosphate ions in a non-apatitic environment. The intensity of this shoulder was maximum at 5 minutes and afterwards it strongly decays with the time. This shoulder disappeared in the spectra of Ap precipitated after 4 hours whereas in the cAp samples, it only disappears for the particles collected after 48 hours.

The width of the ν_4PO_4 band at 603 cm^{-1} was directly correlated to the particles crystallinity degree, *i.e.* the lower this value the higher the crystallinity [35]. Table 3 summarizes the full width at half maximum (FWHM) of this band for the Ap and cAp nanoparticles. According to this parameter, particles increased their crystallinity degree with the precipitation time, Ap being more crystalline than cHA. This trend is in good agreement with the XRPD data (table 1).

The ν_2CO_3 band (at *ca.* 875 cm^{-1}) has been deconvoluted by non-linear fitting (fig. 6a) in order to estimate the intensities of the A-type (880 cm^{-1}) [34], B-type (873 cm^{-1}) [34] and labile (868 cm^{-1}) carbonate bands, *i.e.*, in a non-apatitic environment [24]. The band at 845 cm^{-1} is assignable to the δCOO [36] of the citrate ions. The ratio between the integrated intensities of the different carbonate bands (A-type, B-type and labile) to the total carbonate is plotted in Figure 6(b). Carbonate in B positions was noticeably the most favored situation. A-type substitutions, which were practically negligible at short times, increased progressively with time. The nanoparticles with the highest A-type carbonate content were precipitated at 48 hours. The intensity of the labile carbonate band strongly decreased after 5 minutes being nearly negligible after 48 hours. On the other hand, the carbonate content (%) can be also measured as the area ratio of the ν_2CO_3 (894-862 cm^{-1}) over ν_3PO_4 (1184-910 cm^{-1}) regions [35] This index was plotted as a function of the precipitation time (Figure SP5). The carbonate content increases with time up to 24 hours (Figure

SP5), and then it began to steadily decay. This trend is similar to that observed in TGA experiments (table 2) and it is in agreement with the curve of the calculated activity of CO_3^{2-} in solution (Figure 4).

Figure 7 shows the Raman spectra of Ap and cAp precipitated at 48 hours. The most intense peak appears at *ca.* 960 cm^{-1} which corresponds to ν_1PO_4 mode. It was red-shifted (957 cm^{-1}) in the cAp spectrum due to the carbonate incorporation [37]. In the spectrum of cAp nanoparticles, B-type carbonate band appeared at *ca.* 1070 cm^{-1} (ν_1CO_3) with a shoulder at *ca.* 1103 cm^{-1} due to A-type substitutions [34]. It confirmed that B-type substitutions are the predominant ones in cAp nanoparticles. Moreover, in the Raman spectrum of Ap an intense peak at *ca.* 3570 cm^{-1} corresponding to the apatitic νOH mode can be clearly observed (inset of the Figure 7). On the contrary, this band was less intense in the spectrum collected for the cAp nanoparticles because OH ions were replaced by carbonate groups (A-type substitution). The bands at *ca.* 2930 and 845 cm^{-1} are related to the νCH_2 and the δCOO modes [36], respectively, of citrate anions.

3.4. Non-toxicity of the nanoparticles

The non-toxicity of the cAp and Ap precipitated at 96 hours was also tested in a MTT assay on the 4T1 mouse carcinoma cell line. None of the nanoparticle concentrations assessed, ranging from 1 to 100 μg mL^{-1}, was found to be toxic. On the other hand, the vitality of these cells could be reduced to 25% by incubation with a well-known chemotherapeutic drug such as doxorubicin at a 3 μg mL^{-1} concentration.

4. Discussion

On the basis of the above results, we propose the model schematized in Figure 8 to describe the apatite nanoparticles. They are composed of a well-ordered carbonate-apatitic core covered by a non-apatitic layer composed of calcium, phosphate and carbonate species, citrate and structural water. This structure can be observed in the TEM image (Figure 8) of Ap crystallized at 1 hour. The carbonate-substituted apatite core preferentially grew along the *c*-axis. In the plane (10$\underline{1}$0), the spacing between Ca ions matches with either the spacing between the centers of two neighbor COO^- citrate groups (0.32 nm) or the distance between the two terminal carboxylate of citrate (0.688 nm) [14]. Consequently, citrate strongly bound to the (10$\underline{1}$0) crystal face inhibiting their further growth. Nevertheless, the citrate adsorption on other crystal faces is less favored since Ca distances do not match well with the carboxylate distances of the citrate. Accordingly, after crystal growth, the (10$\underline{1}$0) crystal face became predominant, resulting in thin nanocrystals with plate-like morphology. Rey *et al.* [24, 25] have reported the existence of a non-apatitic hydrated surface layer, which was well developed in freshly formed precipitates. They suggested that upon drying a partial restructuration of the surface hydrated layer occurs, but part of the non-apatitic environments still remains [24, 25].

López-Macipe *et al.* [13] proposed that calcium phosphate heterogeneously nucleates on a previously precipitated sodium citrate salt which acts as temporal template. The role of the template is the stabilization of the primary particles formed by heterogeneous nucleation in nanosized dimensions, minimizing their tendency to grow by

aggregation [38]. By doing so, particles reach smaller sizes than those obtained by conventional precipitation methods [13, 38, 39]. The nucleation process is accompanied by a pH drop and, as a consequence, the subsequent dissolution of the template. Our results suggest that ACP is the first precipitated phase that directly and gradually transforms to HA [40] from the inner toward the outer surface and that this transformation is promoted by the adsorption of free citrate ions on the particle surface which results in the formation of nanoparticles composed of a carbonate-substituted apatitic core embedded on a non-apatitic hydrated layer (Figure 8). From our current experimental data it is not possible to determine the nature, crystalline or amorphous, of the outermost hydrated layer. It could be either a well-structured non-apatitic layer as proposed by Rey *et al.* or, on the other hand, it could be the remaining non-transformed ACP. Indeed, a non-structured surface layer has been previously detected in synthetic apatite by HREM and Solid-State RMN [41-45]. Additionally, recent studies proposed a model of apatitic crystallites embedded in an amorphous matrix to explain the formation of nanocrystalline apatites in dentin of rats [46, 47] and human molars [48]. This amorphous surface layer has been also found in synthetic [49] and biological [50] aragonite.

The high initial concentration of citrate to crystallize nanoapatite by the present thermal decomplexing of Ca/citrate/phosphate/carbonate solutions was chosen to ensure the total complexation of calcium ions in the mother solution. Nevertheless, it is worth to notice that the amount of citrate found on the nanoparticles curiously is very similar to that recently measured in bone apatite by Hu et *al.* [14]. Additionally, the interesting role of citrate temporarily stabilizing the amorphous phase could be comparable to the key roles of macromolecules stabilizing amorphous phase of calcium phosphate in *in vitro* [51] and *in vivo* [11, 12, 52] experiments.

Figure 9 represents the pH of the reaction mixture as a function of the precipitation time in the Ap and cAp preparation. In light of these findings and the previous characterizations, a scheme of the morphological evolution of the Ap and cAp crystals is depicted in Figure 9. In the absence of carbonate, the sudden decrease of the pH up to 6.5 gives rise to a fast dissolution of the non-apatitic hydrated layer. This explains the strong size decrease at the beginning (from 5 minutes to 1 hour). Afterwards, the nanocrystals grow preferentially along the *c*-axis as previously described. On the other hand, in the presence of carbonate, the pH initially decreases to 7.4, then increases up to 8.7 to further undergone a decrease to 7.5. This pH oscillations lead to a slow and gradual dissolution of the hydrated layer with the time which could explain the slightly decrease of the mean length of the cAp with time (Table 1). Moreover, the incorporation of carbonate into the apatitic crystal lattice prevents the growth of the particles along the c-axis [28, 53] thus resulting in shorter and more isometric particles. Moreover, both nanoparticle types appear to be biocompatible since they do not show any sign of toxicity at all the concentrations assessed, up to 100 μg mL^{-1}.

5. Conclusions

In the present work we propose to combine a previously developed thermal decomplexing batch method of Ca-Citrate/phosphate metastable solutions with the addition of Na_2CO_3 to crystallize bone-like carbonate-apatite nanoparticles with controlled carbonation degree, size and crystallinity, containing a non-apatitic hydrated layer stabilized by citrate ions. We precipitated non-stoichiometric poorly crystalline nanoparticles with sizes ranging from 20 to 200 nm and carbonation degree close to the one observed in bone-like apatites. In the absence of carbonate in the initial solution, we obtained larger and more crystalline nanoparticles whereas in the presence of carbonate we found smaller and more isometric nanoparticles. Furthermore, in the latter case, the presence of carbonate in the solution promotes the incorporation of these ions in A and B type positions on the apatitic structure, i.e., replacing OH and PO_4 groups, respectively. Hence, these two experimental conditions play an important role in tailoring both the physicochemical and the morphological properties of nano-apatites such as size, solubility and carbonate content, all of which are quite important to obtain bone-like apatite with potential biomedical applications. In fact, it is well known that the biological properties as well as the behavior of drug-functionalized nanoparticles (mainly load and release properties) are basically controlled by the physico-chemical properties of the nanoparticles such as size, charge and surface chemistry [16]. These properties can be thus be easily tailored by the proposed crystallization method. Additionally, citrate ions were recently demonstrated to stabilize hydrocolloids of hydroxyapatite in water solutions [54]. Ap and cAp nanoparticles appear to be fully biocompatible since none of the concentrations assessed in the MTT, ranging from 1 to 100 μg mL^{-1}, was found to be toxic. Consequently, the nanoparticles can be used as nano-carriers for local targeted drug delivery system as well as biomimetic scaffold based materials in bone replacement.

Acknowledgements

This work was carried out within the framework of the projects Spanish-Italian Integrated Action (IT2009-00028) and MAT2011-28543 (Spanish Ministerio de Ciencia e Innovación (MICINN)). J.G.M. and J.M.D.L. belong to the research team *"Factoría de Cristalización" (Consolider Ingenio 2010)* of the Spanish Ministerio de Ciencia e Innovación. J.M.D.L. and I.R. also thank to the Consejo Superior de Investigaciones Científicas (CSIC) for their postdoctoral JAE-DOC and predoctoral JAE-Pre research contract, respectively. The activity carried out by A.T. was supported by the research project FIRB "BIOPROTESI" (Grant Number: Prot. N. RBIP068JL9) funded by MIUR. Authors also gratefully acknowledge to Dra. Antonella Guagliardi and Dr. Christophe Drouet for the fruitful discussions and revision of the manuscript.

References

[1] Mann S. Biomineralization: principles and concepts in bioinorganic materials chemistry. Oxford: University Press; 2001.

[2] Lowenstam HA, Weiner S. On Biomineralization. Oxford: University Press; 1989.
[3] Eichert C, Drouet C, Sfihi H, Rey C, Combes C. Nanocrystalline apatite-based biomaterials: synthesis, processing and characterization. In: Kendall JB, editor. Biomaterials Research Advances: Nova Science Publishers; 2007. p. 93–143.
[4] Wang L, Nancollas GH. Calcium Orthophosphates: Crystallization and Dissolution. Chemical Reviews 2008;108:4628-69.
[5] Roveri N, Palazzo B. Hydroxyapatite Nanocrystals as Bone Tissue Substitute. Nanotechnologies for the Life Sciences: Wiley-VCH Verlag GmbH & Co. KGaA; 2007.
[6] Dorozhkin SV. Nanosized and nanocrystalline calcium orthophosphates. Acta Biomater 2010;6:715-34.
[7] Tang R, Wang L, Nancollas GH. Size-effects in the dissolution of hydroxyapatite: an understanding of biological demineralization. J Mater Chem 2004;14:2341-6.
[8] Hartles RL. Citrate in Mineralized Tissues. Adv Oral Biol 1964;1:225-53
[9] Gómez-Morales J, Delgado-López JM, Iafisco M, Hernández-Hernández A, Prat M. Amino Acidic Control of Calcium Phosphate Precipitation by Using the Vapor Diffusion Method in Microdroplets. Cryst Growth Des 2011;11:4802-9.
[10] Gericke A, Qin C, Spevak L, Fujimoto Y, Butler WT, Sorensen ES, et al. Importance of phosphorylation for osteopontin regulation of biomineralization. Calcif Tissue Int 2005;77:45-54.
[11] Mahamid J, Sharir A, Addadi L, Weiner S. Amorphous calcium phosphate is a major component of the forming fin bones of zebrafish: Indications for an amorphous precursor phase. Proc Natl Acad Sci USA 2008;105:12748-53.
[12] George A, Bannon L, Sabsay B, Dillon JW, Malone J, Veis A, et al. The Carboxyl-terminal Domain of Phosphophoryn Contains Unique Extended Triplet Amino Acid Repeat Sequences Forming Ordered Carboxyl-Phosphate Interaction Ridges That May Be Essential in the Biomineralization Process. J Biol Chem 1996;271:32869-73.
[13] López-Macipe A, Gómez-Morales J, Rodríguez-Clemente R. Nanosized hydroxyapatite precipitation from homogeneous calcium/citrate/phosphate solutions using microwave and conventional heating. Adv Mater 1998;10:49.
[14] Hu YY, Rawal A, Schmidt-Rohr K. Strongly bound citrate stabilizes the apatite nanocrystals in bone. Proc Natl Acad Sci USA 2010;107:22425-9.
[15] Xie B, Nancollas GH. How to control the size and morphology of apatite nanocrystals in bone. Proc Natl Acad Sci USA 2010;107:22369-70.
[16] Li S-D, Huang L. Pharmacokinetics and Biodistribution of Nanoparticles. Mol Pharm 2008;5:496-504.
[17] Leeuwenburgh SCG, Jo J, Wang H, Yamamoto M, Jansen JA, Tabata Y. Mineralization, Biodegradation, and Drug Release Behavior of Gelatin/Apatite Composite Microspheres for Bone Regeneration. Biomacromolecules 2010;11:2653-9.
[18] Gustafsson JP.Visual MINTEQ 3.0, Computer Program for Calculating Aqueous Geochemical Equilibria; 2011. Adapted from MINTEQA2 (CEAM, EPA, 1999).
[19] Klug HP, Alexander LE. X-Ray Diffraction Procedures: For Polycrystalline and Amorphous Materials. 2nd ed. New York: Wiley-VCH; 1974.
[20] Lazic S. Microcrystalline hydroxyapatite formation from alkaline solutions. J Cryst Growth 1995;147:147-54.
[21] Iafisco M, Gómez-Morales J, Hernández-Hernández MA, García-Ruiz JM, Roveri N. Biomimetic Carbonate-Hydroxyapatite Nanocrystals Prepared by Vapor Diffusion. Adv Eng Mater 2010;12:B218-B23.
[22] Pan HB, Darvell BW. Effect of Carbonate on Hydroxyapatite Solubility. Cryst Growth Des 2010;10:845-50.
[23] Zhang C, Yang J, Quan Z, Yang P, Li C, Hou Z, et al. Hydroxyapatite Nano- and Microcrystals with Multiform Morphologies: Controllable Synthesis and Luminescence Properties. Cryst Growth Des 2009;9:2725-33.
[24] Rey C, Combes C, Drouet C, Sfihi H, Barroug A. Physico-chemical properties of nanocrystalline apatites: Implications for biominerals and biomaterials. Mater Sci Eng C 2007;27:198-205.
[25] Rey C, Combes C, Drouet C, Glimcher MJ. Bone mineral: update on chemical composition and structure. Osteoporos Int 2009;20:1013-21.
[26] Arellano-Jiménez MJ, García-García R, Reyes-Gasga J. Synthesis and hydrolysis of octacalcium phosphate and its characterization by electron microscopy and X-ray diffraction. J Phys Chem Solids 2009;70:390-5.
[27] Roveri N, Palazzo B, Iafisco M. The role of biomimetism in developing nanostructured inorganic matrices for drug delivery. Expert Opin Drug Deliv 2008;5:861-77.
[28] Legeros RZ, Trautz OR, Legeros JP, Klein E, Shirra WP. Apatite Crystallites: Effects of Carbonate on Morphology. Science 1967;155:1409-11.
[29] Baig AA, Fox JL, Hsu J, Wang Z, Otsuka M, Higuchi WI, et al. Effect of carbonate content and crystallinity on the metastable equilibrium solubility behavior of carbonated apatites. J Colloid Interf Sci 1996;179:608-17.
[30] Yao F, LeGeros JP, LeGeros RZ. Simultaneous incorporation of carbonate and fluoride in synthetic apatites: Effect on crystallographic and physico-chemical properties. Acta Biomater 2009;5:2169-77.
[31] Tõnsuaadu K, Gross K, Plõduma L, Veiderma M. A review on the thermal stability of calcium apatites. J Therm Anal Calorim 2011;DOI: 10.1007/s10973-011-1877-y.
[32] Liou SC, Chen SY, Lee HY, Bow JS. Structural characterization of nano-sized calcium deficient apatite powders. Biomaterials 2004;25:189-96.
[33] Koutsopoulos S. Synthesis and characterization of hydroxyapatite crystals: A review study on the analytical methods. J Biomed Mater Res 2002;62:600-12.
[34] Antonakos A, Liarokapis E, Leventouri T. Micro-Raman and FTIR studies of synthetic and natural apatites. Biomaterials 2007;28:3043-54.
[35] Bala Y, Farlay D, Delmas PD, Meunier PJ, Boivin G. Time sequence of secondary mineralization and microhardness in cortical and cancellous bone from ewes. Bone 2010;46:1204-12.

[36] Socrates G. Infrared and Raman Characteristic Group Frequencies. Chichester: John Wiley & Sons; 2001.
[37] Awonusi A, Morris M, Tecklenburg M. Carbonate assignment and calibration in the raman spectrum of apatite. Calcif Tissue Int 2007;81:46-52.
[38] Rodríguez-Clemente R, López-Macipe A, Gómez-Morales J, Torrent-Burgués J, Castaño VM. Hydroxyapatite precipitation: A case of nucleation-aggregation-agglomeration-growth mechanism. J Eur Ceram Soc 1998;18:1351-6.
[39] Dey A, Bomans PHH, Muller FA, Will J, Frederik PM, de With G, et al. The role of prenucleation clusters in surface-induced calcium phosphate crystallization. Nat Mater 2010;9:1010-4.
[40] Tsuji T, Onuma K, Yamamoto A, Iijima M, Shiba K. Direct transformation from amorphous to crystalline calcium phosphate facilitated by motif-programmed artificial proteins. Proc Natl Acad Sci USA 2008;105:16866-70.
[41] Sakhno Y, Bertinetti L, Iafisco M, Tampieri A, Roveri N, Martra G. Surface Hydration and Cationic Sites of Nanohydroxyapatites with Amorphous or Crystalline Surfaces: A Comparative Study. J Phys Chem C 2010;114:16640-8.
[42] Isobe T, Nakamura S, Nemoto R, Senna M, Sfihi H. Solid-State Double Nuclear Magnetic Resonance Study of the Local Structure of Calcium Phosphate Nanoparticles Synthesized by a Wet-Mechanochemical Reaction. J Phys Chem B 2002;106:5169-76.
[43] Jäger C, Welzel T, Meyer-Zaika W, Epple M. A solid-state NMR investigation of the structure of nanocrystalline hydroxyapatite. Magn Reson Chem 2006;44:573-80.
[44] Bertinetti L, Tampieri A, Landi E, Ducati C, Midgley PA, Coluccia S, et al. Surface Structure, Hydration, and Cationic Sites of Nanohydroxyapatite:¸Äâ UHR-TEM, IR, and Microgravimetric Studies. J Phys Chem C 2007;111:4027-35.
[45] Nassif N, Martineau F, Syzgantseva O, Gobeaux F, Willinger M, Coradin T, et al. In Vivo Inspired Conditions to Synthesize Biomimetic Hydroxyapatite. Chem Mater 2010;22:3653-63.
[46] Tseng Y-H, Tsai Y-L, Tsai TWT, Chao JCH, Lin C-P, Huang S-H, et al. Characterization of the Phosphate Units in Rat Dentin by Solid-State NMR Spectroscopy. Chem Mater 2007;19:6088-94.
[47] Huang S-J, Tsai Y-L, Lee Y-L, Lin C-P, Chan JCC. Structural Model of Rat Dentin Revisited. Chem Mater 2009;21:2583-5.
[48] Porter AE, Nalla RK, Minor A, Jinschek JR, Kisielowski C, Radmilovic V, et al. A transmission electron microscopy study of mineralization in age-induced transparent dentin. Biomaterials 2005;26:7650-60.
[49] Nassif N, Gehrke N, Pinna N, Shirshova N, Tauer K, Antonietti M, et al. Synthesis of Stable Aragonite Superstructures by a Biomimetic Crystallization Pathway. Angew Chem 2005;117:6158-63.
[50] Nassif N, Pinna N, Gehrke N, Antonietti M, Jäger C, Cölfen H. Amorphous layer around aragonite platelets in nacre. Proc Natl Acad Sci USA 2005;102:12653-5.
[51] Zhong C, Chu CC. Biomimetic mineralization of acid polysaccharide-based hydrogels: towards porous 3-dimensional bone-like biocomposites. J Mater Chem 2012;22:6080-7.
[52] Beniash E, Metzler RA, Lam RSK, Gilbert PUPA. Transient amorphous calcium phosphate in forming enamel. J Struct Biol 2009;166:133-43.
[53] LeGeros RZ. Apatites in biological systems. Prog Cryst Growth Charact 1981;4:1-45.
[54] Li CC, Zhao LP, Han JJ, Wang RF, Xiong CD, Xie XY. Synthesis of citrate-stabilized hydrocolloids of hydroxyapatite through a novel two-stage method: A possible aggregates-breakdown mechanism of colloid formation. J Colloid Interf Sci 2011;360:341-9.

Figure and table list

Figure 1. Calculated activities as a function of the temperature, of the main ionic and neutral species in the mother solution (pH=8.5) without Na_2CO_3 (a) and with 50 mM Na_2CO_3 (b). Note: Cit=$C_6H_5O_7$.

Figure 2. TEM micrographs of Ap crystallized after 5 minutes (a), 2 hours (c) and 96 hours (e) and cAp crystallized after 5 minutes (b), 2 hours (d) and 96 hours (f). Insets show the SAED pattern collected for each sample. The scale bars are 200 nm.

Figure 3. XRPD patterns of (a) Ap crystallized after 5 minutes (black line) and 96 hours (red line) and (b) cAp crystallized after 5 minutes (black line) and 96 hours (red line).

Figure 4. Calculated activity as a function of the precipitation time of the main carbonate species in the mother solution in the presence of Na_2CO_3 at 80ºC. The activities were calculated with Visual MINTEQ 3.0 speciation software[18].

Figure 5. FTIR spectra of cAp crystallized after 5 minutes (black line) and 48 hours (red line).

Figure 6. (a) Non-linear curve fitting of the cAp bands in the ν_2CO_3 spectral region. (b) Plot as a function of the precipitation time of the ratio between the integrated intensities of the A-type, B-type and labile carbonate bands to the total intensity of the ν_2CO_3 band.

Figure 7. Raman spectra of cAp (black line) and Ap (red line) crystallized at 48 hours. The inset shows an enlarge view of the typical OH and CH stretching modes spectral region.

Figure 8. Proposed model of the apatite nanoparticle composed of a well-ordered apatite core covered by a non-apatitic hydrated layer composed of ionic species, including citrate, and structural water. TEM image shows this layered structure.

Figure 9. pH evolution of the reaction mixture during the Ap and cAp crystallization. The morphological evolution of the Ap and cAp crystals are also schematized.

Table 1. Mean Length (L), mean width (W) and mean aspect ratio (R) of Ap and cAp nanoparticles at different precipitation times. Average size of crystal domains along the [0,0,2] and [3,1,0] directions of Ap and cAp at different precipitation times, calculated applying the Scherrer equation.

Precipitation time	L[a] [nm]	W[a] [nm]	R[a]	$D_{[002]}$[nm]	$D_{[310]}$[nm]	$D_{[002]}$/ $D_{[310]}$
Ap 5 minutes	98.6±29.5	21.2±4.6	4.7±1.2	19.4	4.0	4.8
Ap 1 hour	44.7±24.5	11.7±6.6	4.0±1.3	37.1	5.9	6.3
Ap 2 hours	74.6±26.5	14.8±5.6	5.5±2.4	48.0	6.3	7.6
Ap 4 hours	84.8±16.2	15.7±3.8	5.6±1.3	45.3	6.5	7.0
Ap 24 hours	83.6±32.0	13.7±6.1	6.9±3.0	48.0	8.6	5.6
Ap 96 hours	104±43.2	14.8±5.8	7.6±3.2	90.6	9.6	9.4
cAp 5 minutes	108.7±15.7	26.6±5.3	4.3±1.3	17.0	5.2	3.3
cAp 1 hour	48.5±18.4	9.9±5.2	5.4±1.9	22.6	5.9	3.8
cAp 2 hours	59.9±23.7	16.8±6.2	3.7±1.3	30.2	5.6	5.4
cAp 4 hours	54.8±10.1	17.5±3.3	3.2±0.9	35.4	6.1	5.8
cAp 24 hours	40.4±15.1	11.6±3.0	3.7±1.5	31.3	5.7	5.5
cAp 96 hours	29.2±10.7	12.3±2.8	2.5±1.0	45.3	8.0	5.7

[a] Measured from TEM micrographs. The mean value and the standard deviation were calculated measuring the sizes of 100 particles from different experiments.

Table 2. Compositional features and bulk Ca/P of Ap and cAp at different precipitation times.

Precipitation time	Structural water[a] (%wt.)	Citrate[a] (%wt.)	Carbonate[a] (%wt.)	Ca/P[b]
Ap 5 minutes	5.8±0.2	5.0±0.2	1.5±0.2	1.53±0.02
Ap 4 hours	3.9±0.1	2.4±0.1	1.1±0.1	1.51±0.02
Ap 24hours	3.3±0.1	1.9±0.1	1.0±0.1	1.52±0.03
Ap 48 hours	2.9±0.2	2.1±0.2	1.3±0.2	1.53±0.01
Ap 96 hours	2.6±0.2	2.0±0.1	1.0±0.1	1.54±0.02
cAp 5 minutes	6.3±0.3	5.9±0.2	1.5±0.1	1.60±0.02
cAp 4 hours	3.8±0.3	3.3±0.2	1.5±0.1	1.60±0.02
cAp 24hours	3.6±0.2	3.5±0.2	3.1±0.2	1.59±0.02
cAp 48 hours	2.6±0.2	2.1±0.1	2.6±0.3	1.59±0.01

cAp 96 hours	2.5±0.1	2.1±0.1	2.9±0.2	1.58±0.01

[a] Calculated by TGA, [b] Calculated by ICP-OES.

Table 3. Full width at half maximum (FWHM) of the v4PO4 peak (603 cm-1) of Ap and cAp at different precipitation times.

Precipitation time	FWHM (cm^{-1})	
	Ap	cAp
5 minutes	14.3	14.9
1 hour	12.9	13.6
4 hours	12.5	12.9
24 hours	11.2	13.3
48 hours	10.9	11.9
96 hours	9.6	10.5

Graphical Abstract

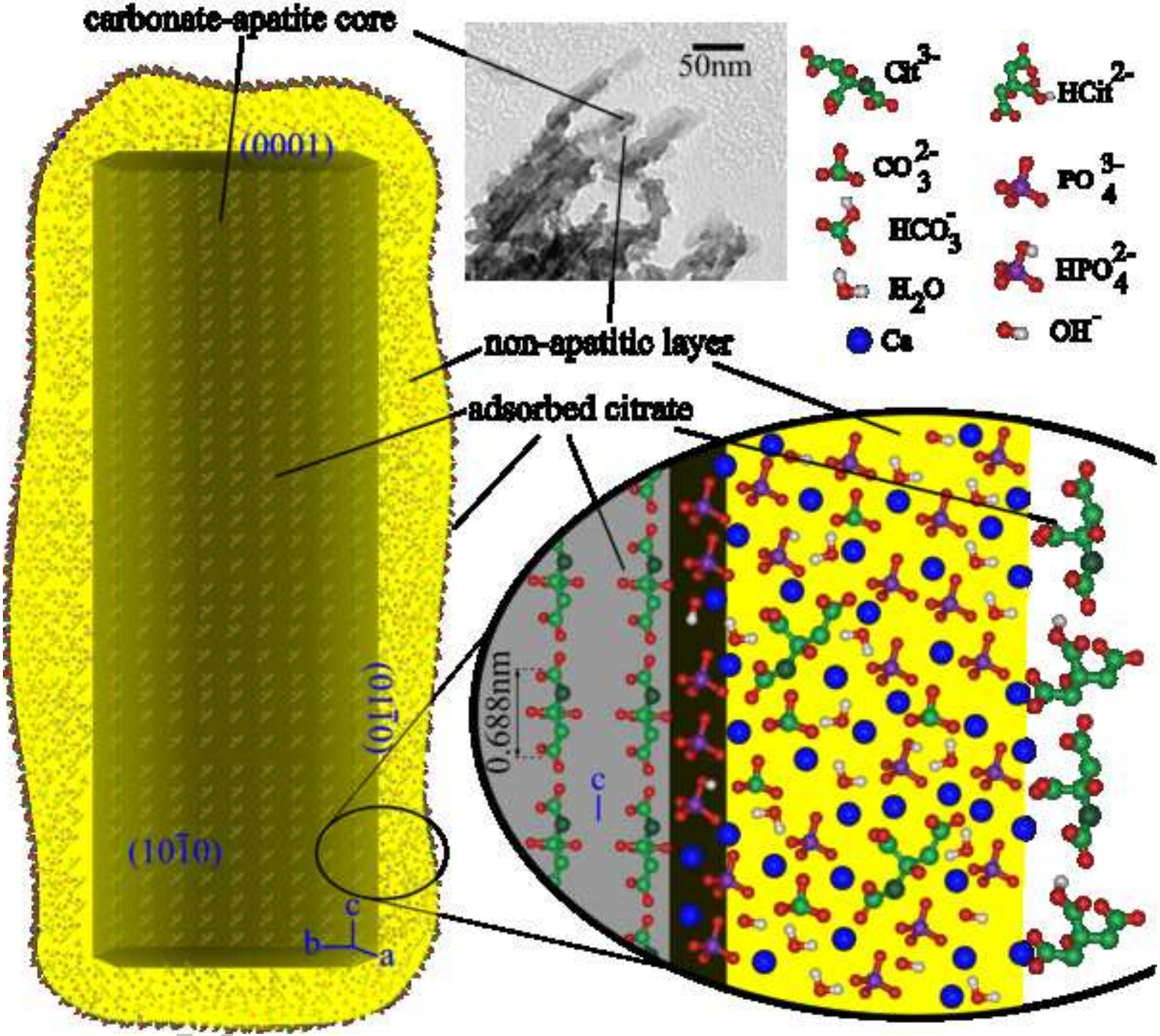

Figure1

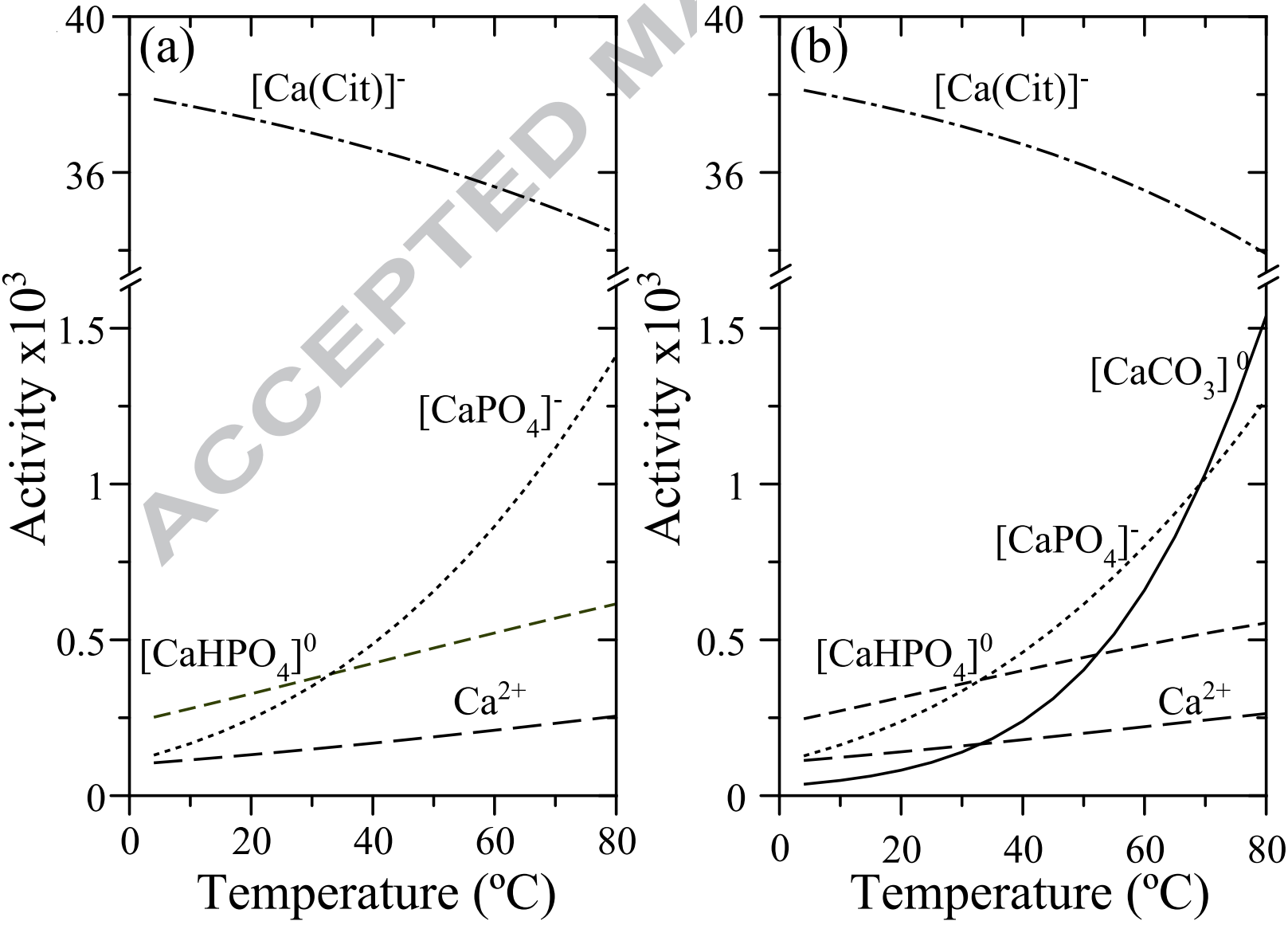

Figure2

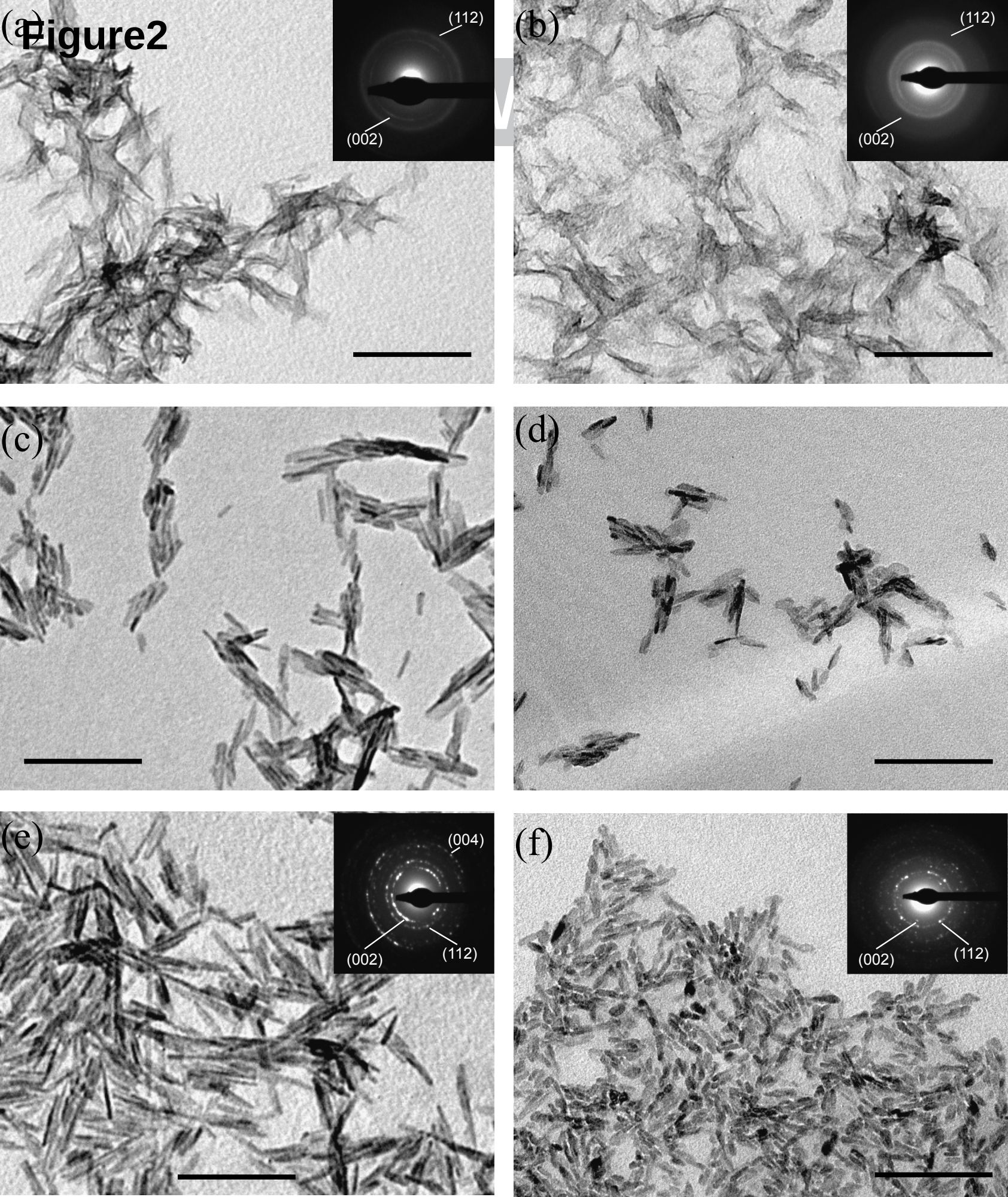

Figure3

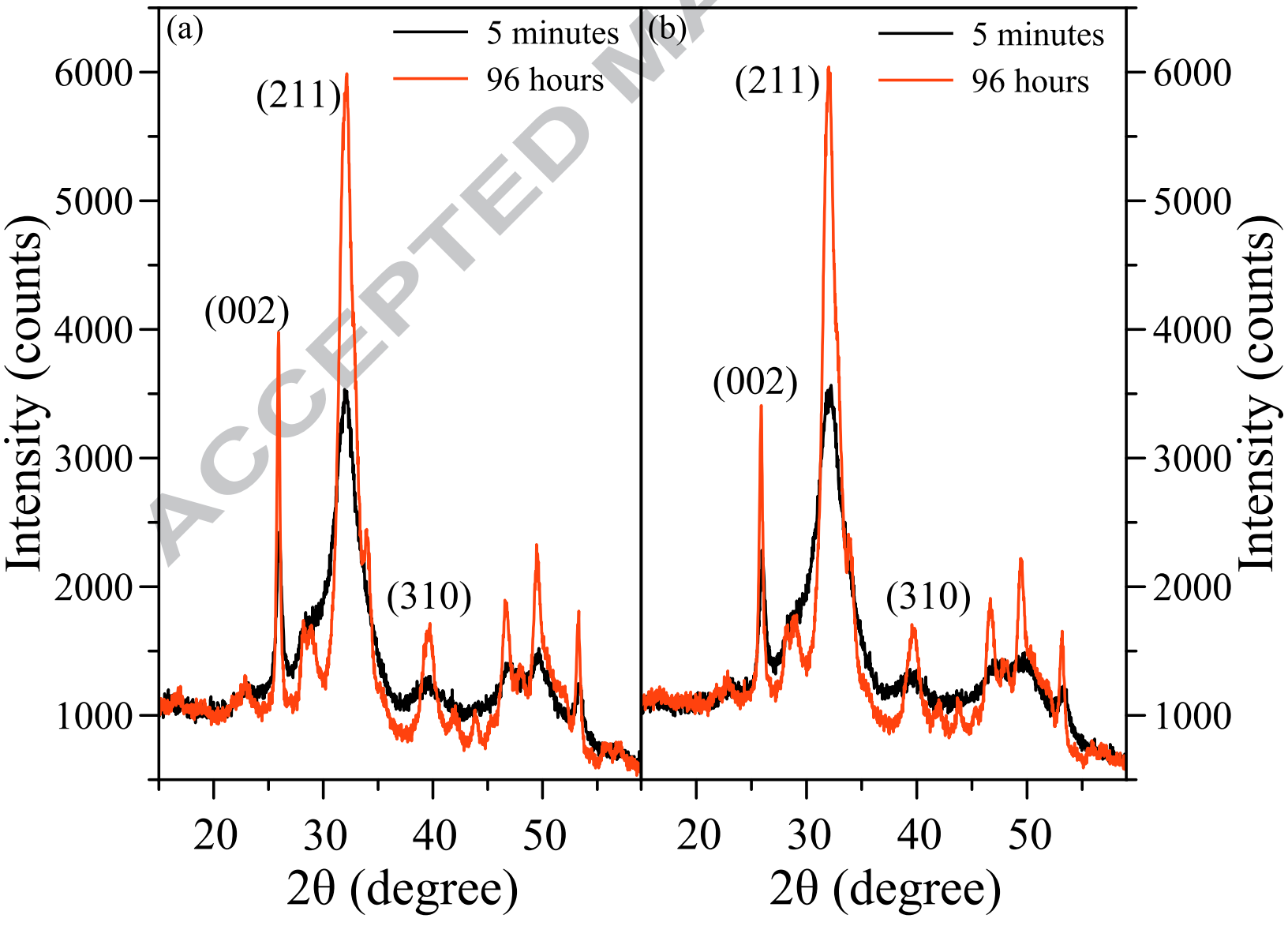

Figure4

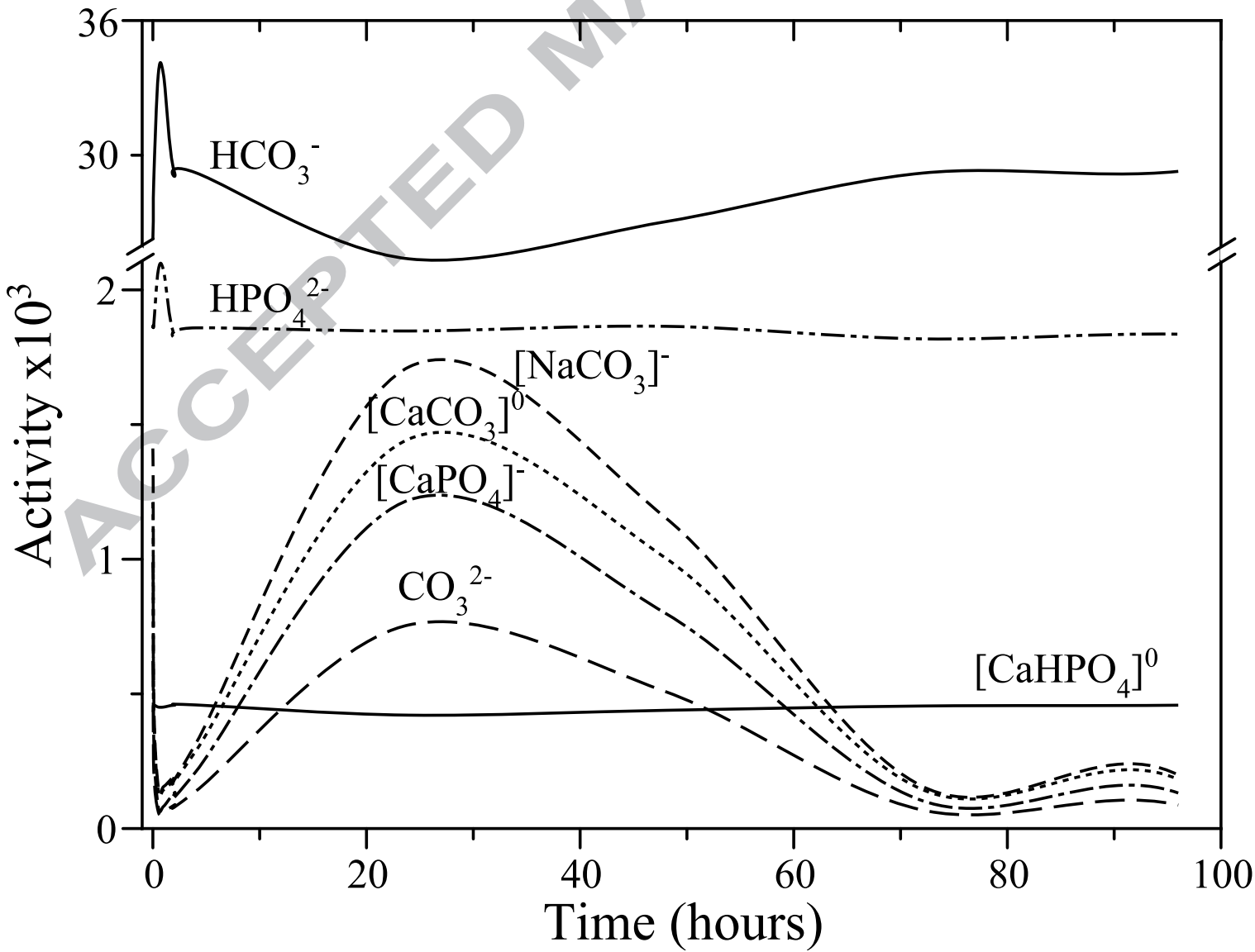

Figure5

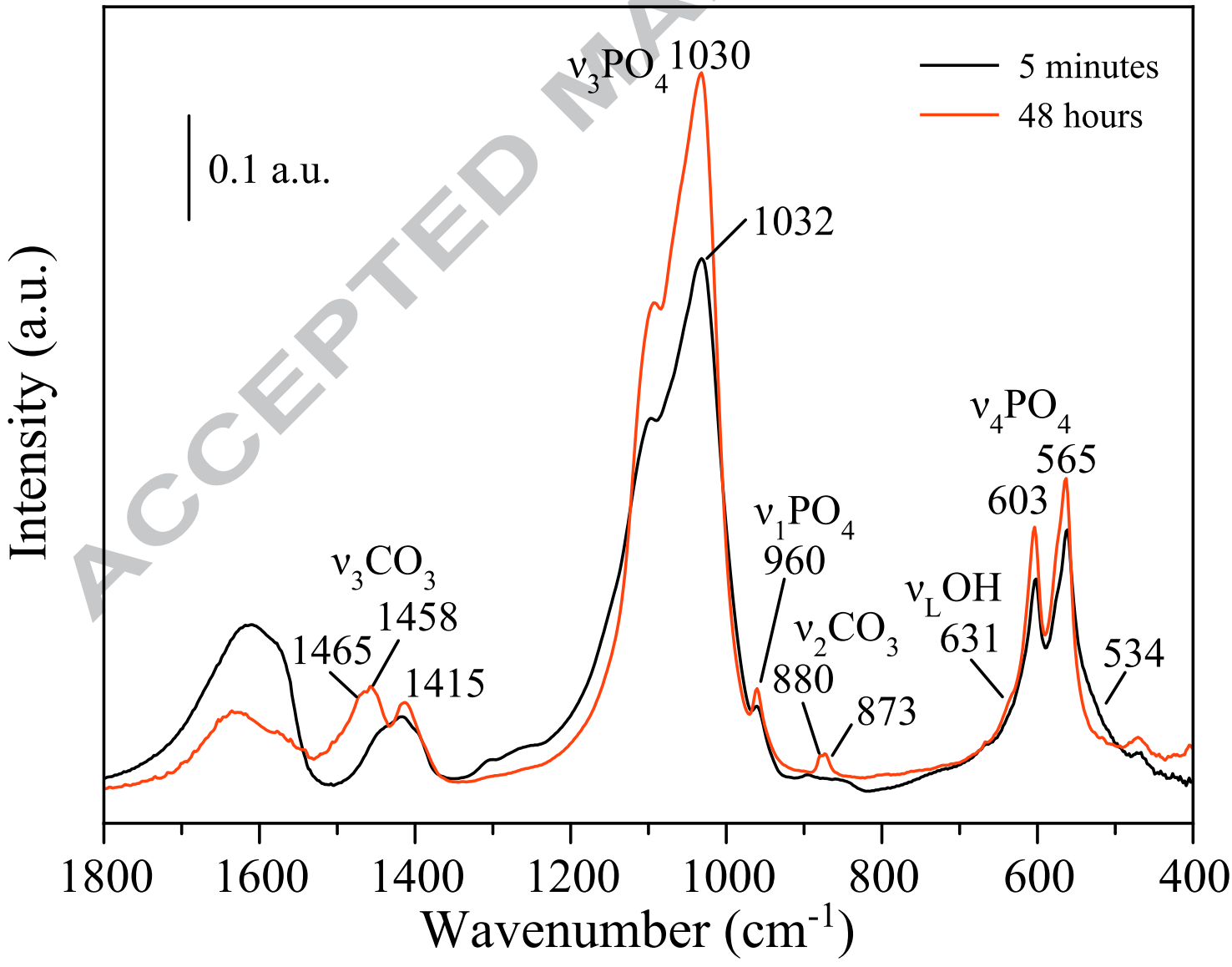

Figure6

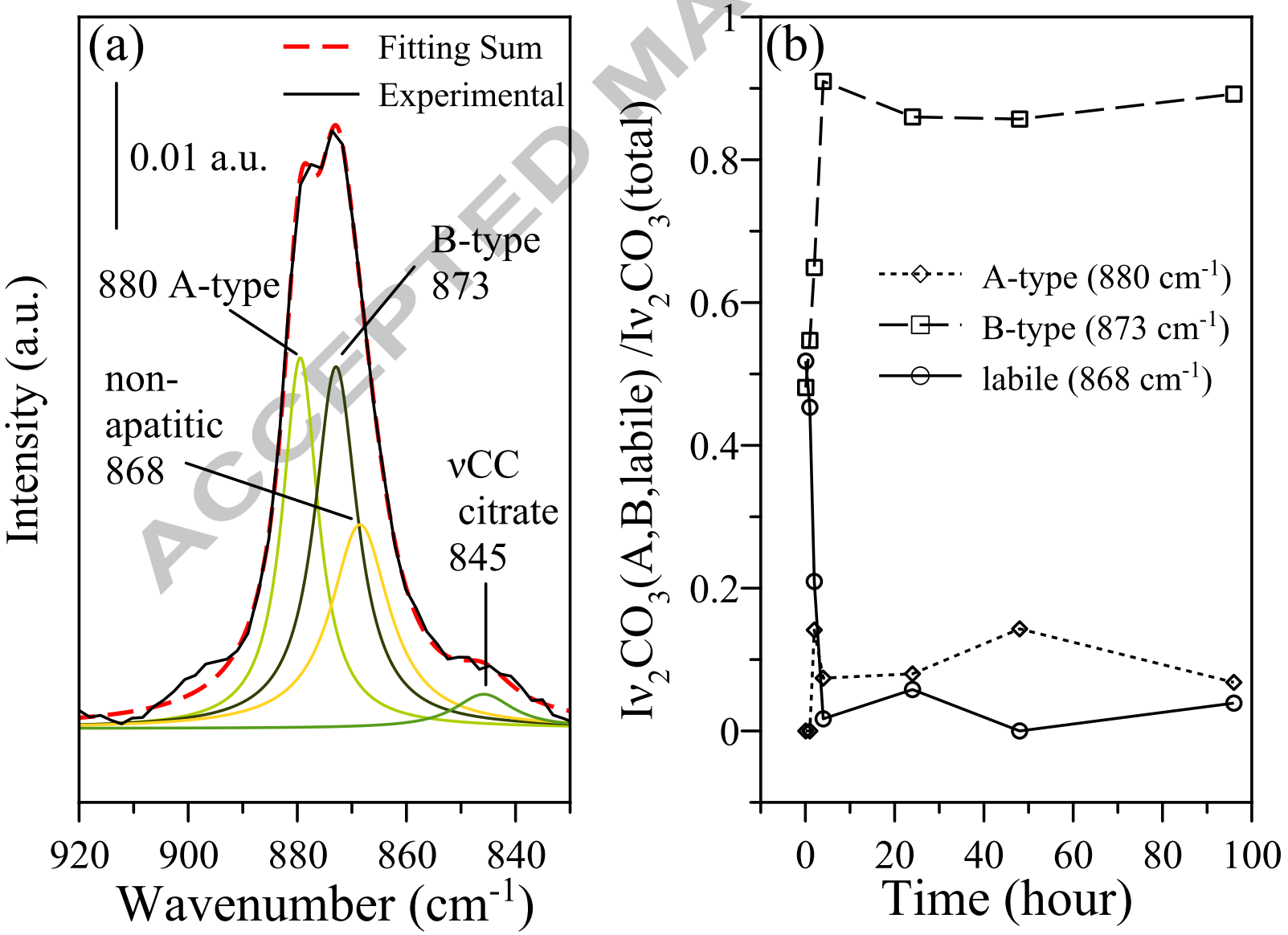

Figure7

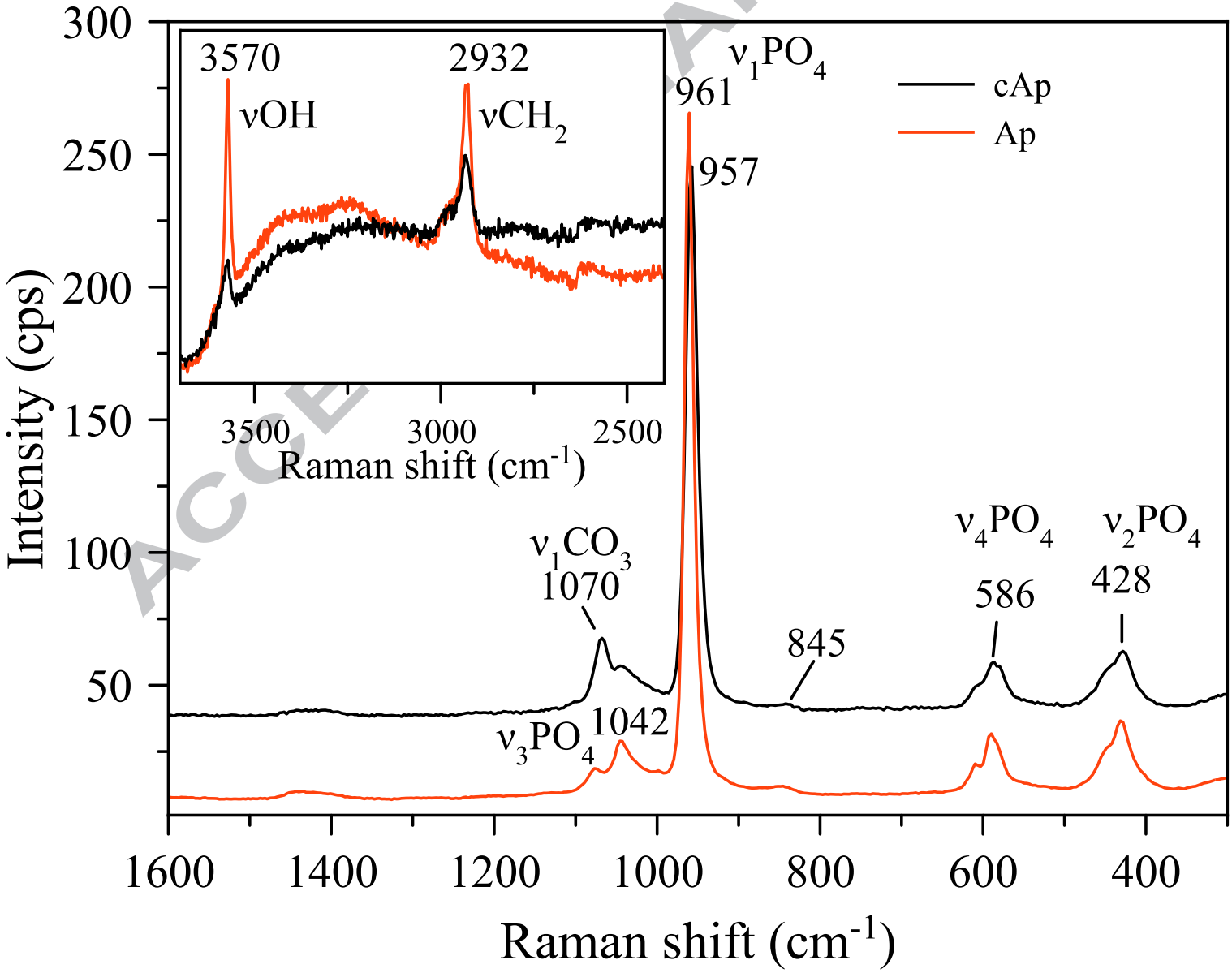

Figure8

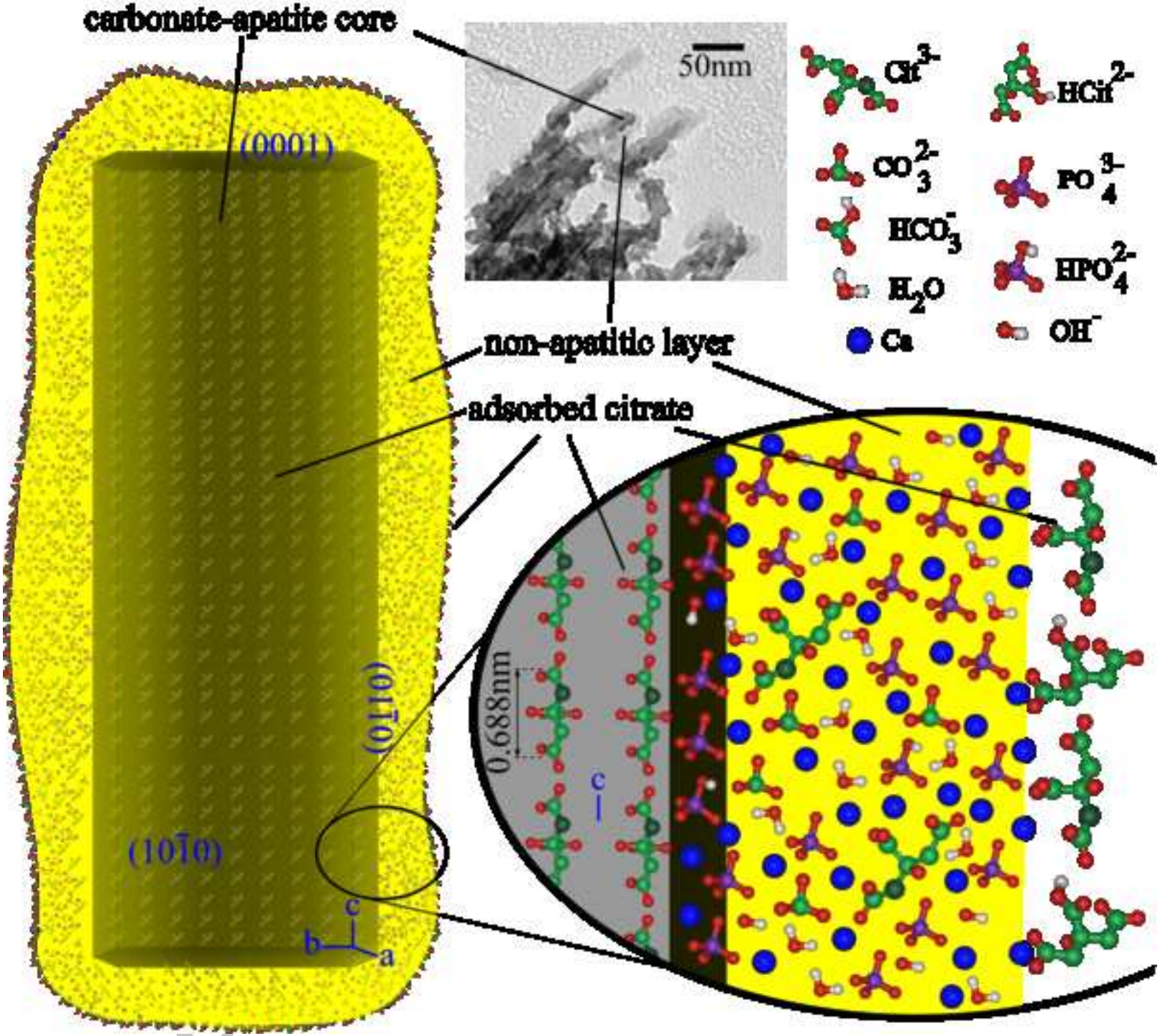

Figure9

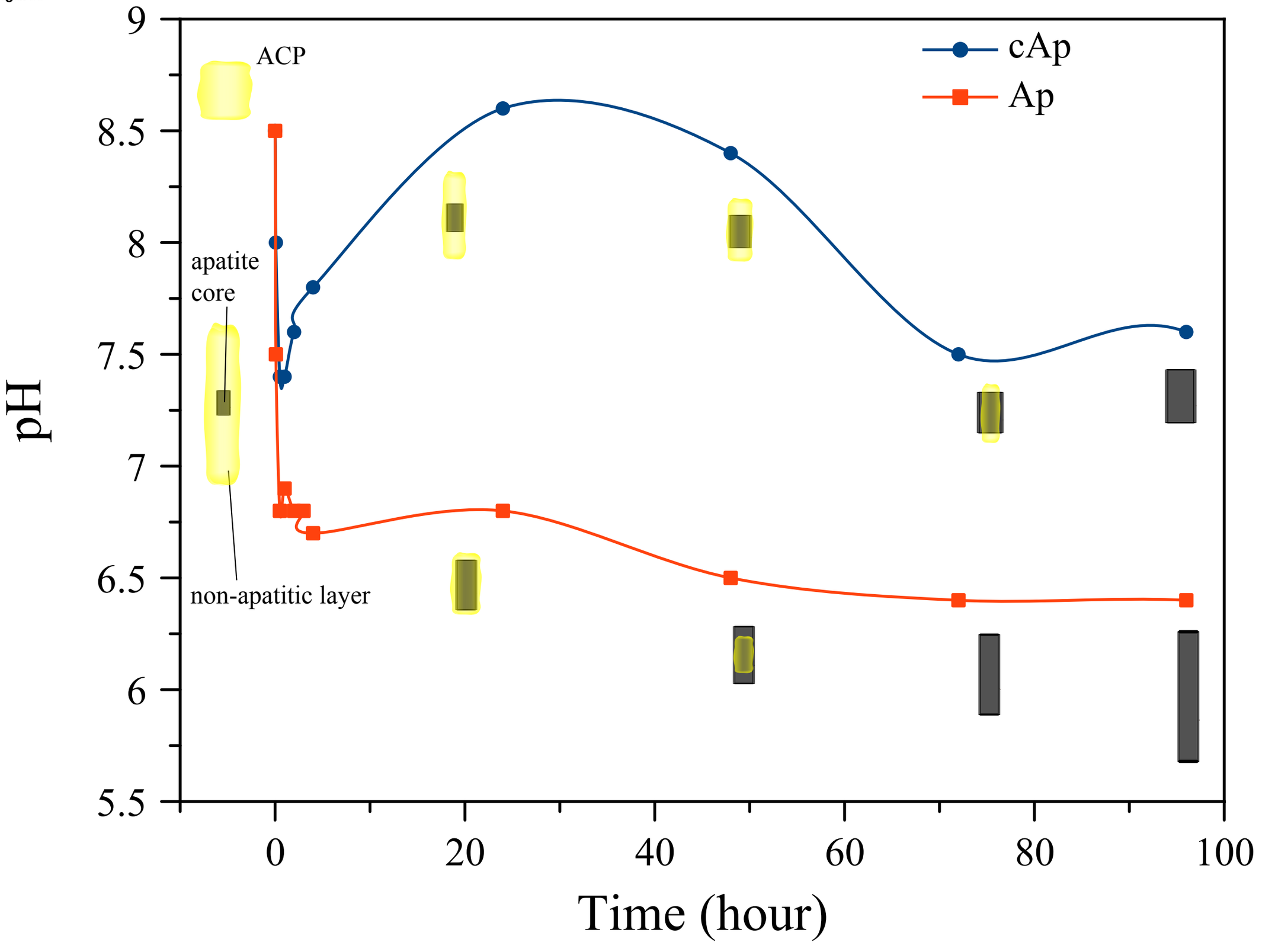
ACP
cAp
Ap
apatite
core
non-apatitic layer
pH
9
8.5
8
7.5
7
6.5
6
5.5
0
20
40
60
80
100
Time (hour)